Pergamon

0301-9322(94)00079-4

*Int. J. Multiphase Flow* Vol. 21, No. 3, pp. 381–404, 1995

0301-9322/95 $9.50 + 0.00

# INVESTIGATION OF BUBBLE FLOW DEVELOPMENTS AND ITS TRANSITION BASED ON THE INSTABILITY OF VOID FRACTION WAVES

CHUL HWA SONG†,[1] HEE CHEON NO[1] and MOON KI CHUNG[2]

[1]Department of Nuclear Engineering, Korea Advanced Institute of Science and Technology, 373-1 Gusung-dong, Yusung-ku, Taejon 305-701, Korea
[2]Thermal Hydraulics Department, Korea Atomic Energy Research Institute, Yusung, P.O. Box 105, Taejon 305-600, Korea

*(Received 7 December 1993; in revised form 24 October 1994)*

**Abstract**—The developments of bubble flow structures and their effect on the propagation properties of void fraction waves are experimentally investigated in vertical upwards, air–water flow. The bubble-to-slug flow regime transition (BSFRT) is investigated based on the instability of the void fraction waves. A series of tests are performed by systematically varying the bubble size for different flow conditions. Several statistical parameters are evaluated from the void fraction signals to objectively characterize the developing flow structures and to investigate the wave propagation properties. In particular, the degree of spatial growth of the void fraction waves is quantified in terms of the spatial attenuation factor (SAF). Two distinct modes of flow structural developments in bubbly flow are observed which are dependent on the bubble size. It is also shown that the different features of wave propagation properties are mainly due to the differences in the developing mode of the flow structures. It turns out that BSFRT is associated with both the instability of void fraction waves and the abrupt changes of the apparent time scale, and the neutral stability condition of the void fraction waves corresponds to the appearance of large structures of the gas phase.

*Key Words*: bubbly flow, bubble size, flow structures, void fraction waves, wave instability

## 1. INTRODUCTION

The discrete nature of two-phase flow causes natural fluctuations in flow parameters, and their statistical treatment may help us to understand and analyze the behavior of two-phase flow. In particular, fluctuations of void fraction reveal the characteristics of the structures of the discrete phase in two-phase flow.

Much attention has been paid to void fraction waves since propagation of void disturbances represent the essential features of bubble flow structures. Several experimental works on void fraction waves have been performed. Most were aimed at obtaining information on the closure law of the two-phase flow model, and on the dispersion of wave propagation by imposing artificial perturbation on the bubble flow. An excellent review of previous works is described by Bouré (1988). Only a few recent works cover the bubble-to-slug flow regime transition (BSFRT) region; these include Matuszkiewicz *et al.* (1987), Tournaire (1987), Saiz-Jabardo & Bouré (1989), Kytömaa & Brennen (1991) and Park *et al.* (1993).

Most previous works observed that void fraction waves are attenuated for bubbly flow, but their attenuation decreases as the mean void fraction increases and is affected by the mixture flow rate. Matuszkiewicz *et al.* (1987) and Saiz-Jabardo & Bouré (1989) proposed the existence of a close relation between the instability of void fraction waves and BSFRT from the experiments in nitrogen–water flow, occurring at a void fraction of $\epsilon = 0.35$–$0.45$. Park *et al.* (1993) confirmed this relation for oil–air flow in annulus at very low velocity conditions, but they showed that it occurs at about $\epsilon = 0.10$. Also, they observed that the waves are slowly amplified with void fraction. Kytömaa & Brennen (1991) observed that the instability of void fraction waves occurs at a void

†Present address: Korea Atomic Energy Research Institute, Thermal Hydraulics Department, Yusung, P.O. Box 105, Taejon 305-600, Korea.

fraction of about $\epsilon = 0.45$. In these previous works, however, no detailed measurements of the wave amplification/attenuation were taken to link it with BSFRT over a wide range of flow conditions.

Previous BSFRT criteria were determined based upon the assumption that the "critical" void fraction, at which BSFRT occurs, is in the range of $\epsilon = 0.25$–$0.3$, and/or obtained based upon a typical mechanism to govern the flow structures (Taitel 1990). These include Taitel *et al.* (1980), Mishima & Ishii (1984) and Kelessidis & Dukler (1989), and previous tools of regime discrimination were mainly based upon visual observations.

The fact that previous works on critical void fraction and void fraction waves show discrepancies between the different investigations might be attributed to two reasons: one is the unidentified effect of the parameters which influence the flow structures and the regime transition mechanism but are not taken into account in experiments nor for physical modelling, and the other is the inaccuracies in the measuring devices.

Recently, Serizawa *et al.* (1991) and Liu (1991) observed that there exists a strong dependence of radial void profiles on bubble size even under fixed flow conditions and the turbulence structures of the liquid phase are clearly affected by bubble size. Liu (1993) also observed that the flow regime transition is very sensitive to the variation of bubble size. Previous works on BSFRT and/or void fraction waves did not, however, consider the bubble size effect, nor separate it from the other effects since, in almost all of the previous works, the size of the bubbles produced is dependent on gas flow, that is, they become gradually larger as gas flow is increased.

The main objectives of the present work are to identify the effect of initial bubble size on the developing mode of bubble flow structures by the statistical processing of void signals, and to observe how it affects the mechanism of slug formation and the BSFRT boundary.

New observations on the wave propagation properties are also presented. It is clarified that the different features of the wave propagation properties originate mainly from the differences in the developing mode of the bubble flow structures; and it is shown, from detailed measurements of the wave damping, that the neutral stability condition of the void fraction waves indicates BSFRT.

## 2. EXPERIMENTAL SET-UP AND INSTRUMENTATIONS

A schematic diagram of the air–water loop is shown in figure 1. The test section, of which the height is about 3 m and the inside diameter is 25 mm, is vertical and transparent. The flow rate of filtered city water is measured by two turbine flow meters installed in parallel. Its temperature is controlled by a heat exchanger. A set of four rotameters with fine metering valves is installed to measure the gas flow coming from the central air supply system.

The bubble generator, as shown in figure 2, is specially designed so as to change the bubble size without varying the other test conditions. The air chamber wall contains 36 holes with 0.4 mm in diameter. Various sizes of bubbles can be generated by varying the nozzle water flow rate which causes the pressure difference between two sides of the air chamber wall (Serizawa *et al.* 1991). The loop is pressurized to 4 bars to avoid the effect of the difference in hydrostatic heads along the channel on the bubble growth, and the system pressure is regulated by continuously purging the exhaust air in the air separator.

An impedance void meter (IVM) is developed to measure the void fraction, as in recent works (e.g. Matuszkiewicz *et al.* 1987; Saiz-Jabardo *et al.* 1989; Delhaye *et al.* 1987, Tournaire 1987; Kytömaa 1991). It consists of a main sensor, a reference sensor and a signal processor. A main sensor, flush-mounted to the inner wall of the test section, consists of two measuring electrodes, facing each other, and four guard electrodes. Two guard electrodes are installed at each side of a measuring electrode in order to evenly distribute the electrical fields in the measuring volume, and thereby minimize the effect of the phase distributions in a measuring volume on the IVM response. The arc ratio of the electrode portion is adopted to be half of the channel inner circumference, which is the value chosen to best avoid the phase distribution effect (Tournaire 1987). Both the measuring electrodes and guard electrodes are excited by the same frequency of 10 kHz with which the role of capacitance is negligible. Here, it is emphasized that the guard electrodes are electrically shielded in order not to influence the output signal, but to play their basic role of minimizing the phase distribution effect which could be caused by the edge effect and the cross-talk problem (Snell *et al.* 1979). The drift in void signals, which may be caused by the changes

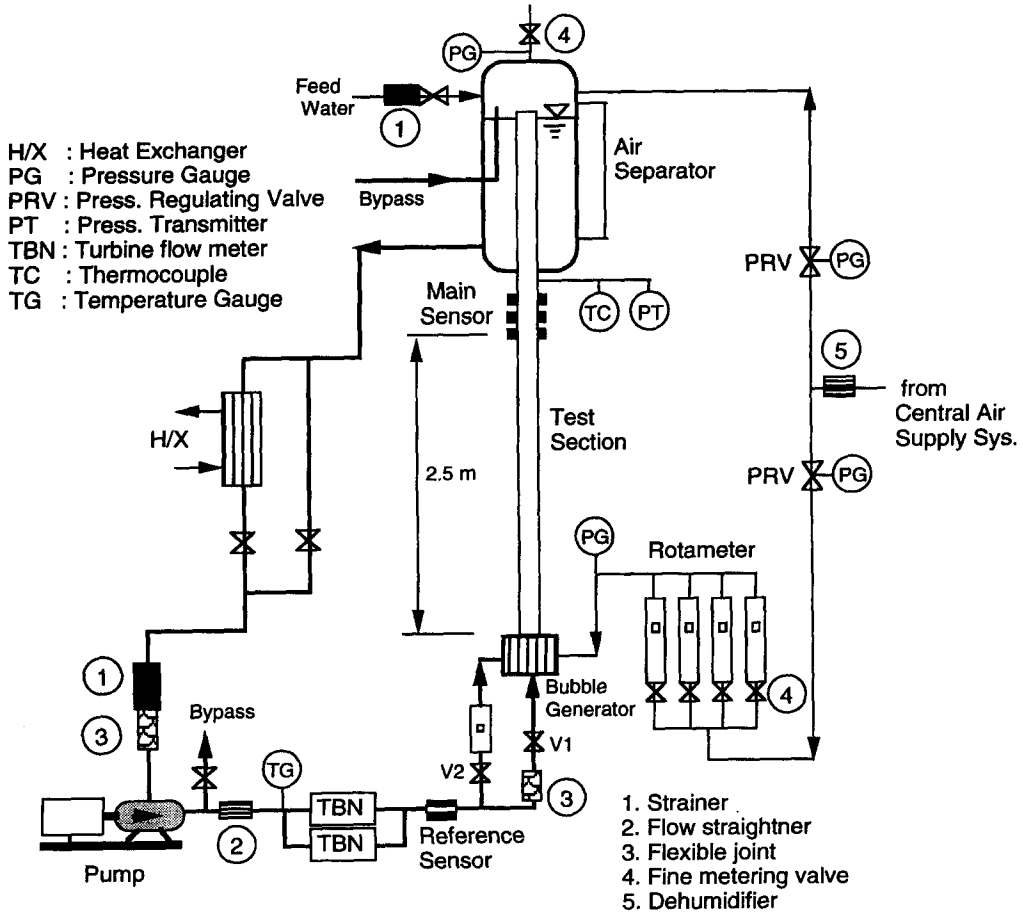


Figure 1. Schematic diagram of the air–water loop.

in the electrical properties of the working fluid, can also be removed by normalizing the main sensor signal by the signal of the reference sensor in the signal processor. The reference sensor is located upstream of the bubble generator, where only water flows. The signal processor with three channels is designed so as to eliminate the inherent errors in the phase difference between channels because it could cause a bias error (limited below 0.15% in the present study) in measured wave propagation properties.

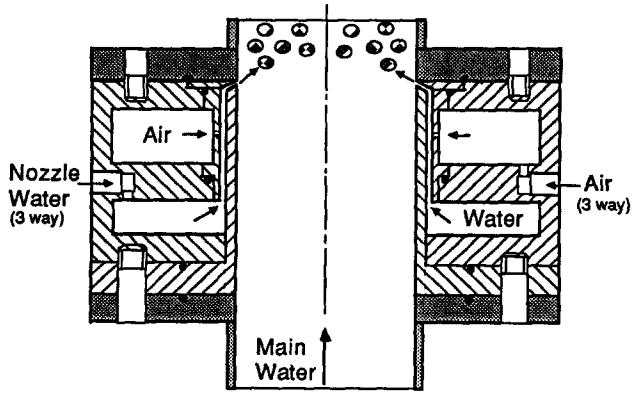


Figure 2. Cross-section of the bubble generator.

In the present measurements, three main sensors are used to measure the void fraction at 2.5 m from the outlet of the bubble generator to ensure that the flow is fully developed (Liu 1993; Qazi *et al.* 1993). The relative short width (10 mm) of the measuring electrode is used for detecting the void fraction waves with short wavelength as well as for obtaining sufficient sensitivity to small changes in void fraction. The distance between two successive main sensors is chosen to be 70 mm to meet the necessity of distinguishing void fraction waves with a relatively long wavelength.

The IVM is calibrated at 4 bars by measuring the two-phase pressure drop between two locations upstream and downstream of the main sensor for low flow conditions where the frictional and accelerational pressure drops are negligibly small (Delhaye *et al.* 1987). The calibration results are curve-fitted as follows:

$$V/V_0 = 0.996 - 1.674\epsilon + 0.134\epsilon^2, \quad [1]$$

where $V$ and $V_0$ are the IVM signals at the void fraction of $\epsilon$ and zero, respectively, and $V/V_0$ corresponds to the conductance ratio. The results are shown in figure 3 which clearly shows the shielding effect of guard electrodes. The case without shielding overestimates the void fraction due to the non-uniform electrical fields in the measuring volume. There are, however, some scattering of the data at a high void region where much more non-uniformity of phase distributions occurs than at a low void region. The calibration curve is also compared with the theoretical predictions of Bruggeman (1935) and Jefferey (1973) (see Turner 1976).

The data acquisition system consists of a 16-bit A/D converter (Data Translation, DT-2829) and a personal computer. The bubble size is measured at the inlet ($L/D = 10$) of the test channel by analyzing the video images taken by the high-speed video motion analyzer (Kodak EktaPro). The image plane is intensified by the light sheet projector (Aerometrics, LVS-170) connected to a 5 W Ar–ion laser source. The light sheet is used not only to avoid the overlapping of bubbles at different planes in the videographic image, but also to easily observe the radial void profiles. The measured bubble size is corrected to compensate for the channel curvature effect on the sizing. The characteristics of the bubbles considered herein are summarized in table 1 with their standard deviations which also include variations due to the effect of gas and liquid flow rates on the bubble size.

A series of tests is performed under the following test conditions:

- liquid superficial velocity: $J_L = 0.12$, 0.18, 0.275, 0.49 m/s,
- void fraction: $\epsilon = 0.03$–0.5,
- bubble diameter: $D_b = 2.7$, 3.2, 3.8, 4.2, 4.8 mm.

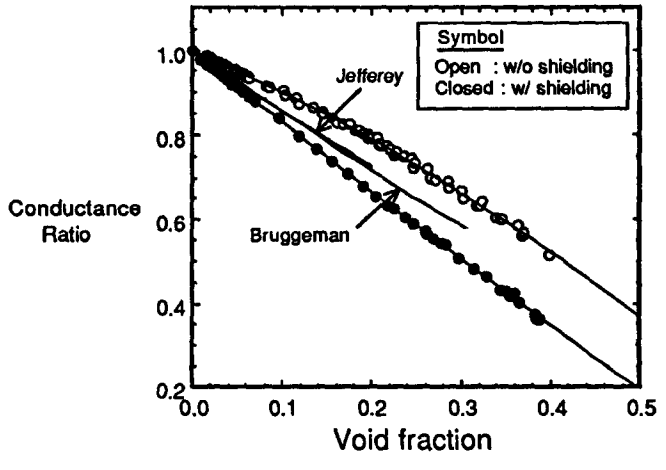


Figure 3. Calibration curve of the impedance void meter.

Table 1. Bubble sizes considered in the present work

| No. | Nozzle water velocity $U_n$† [m/s] | Bubble size, $D_b$‡ Mean (mm) | SD (%) | Bubble sphericity§ (%) |
|---|---|---|---|---|
| 1 | 4.2 | 4.8 | 7.9 | 63.3 |
| 2 | 5.6 | 4.2 | 8.2 | 64.2 |
| 3 | 6.9 | 3.8 | 7.7 | 77.6 |
| 4 | 9.1 | 3.2 | 5.8 | 90.7 |
| 5 | 15.1 | 2.7 | 6.3 | 96.4 |

†The water velocity in the annulus region of the bubble generator.
‡The volume-equivalent diameter of the ellipsoidal-shaped bubble.
§The diameter ratio of the minor to major axis.

## 3. STATISTICAL SIGNAL PROCESSING

The instantaneous signals from three void sensors are simultaneously measured and then statistically processed to determine the signal-to-noise ratio (SNR), probability density function (PDF) and the propagation properties of the void fraction waves. An instantaneous void signal, $\tilde{V}_i(t)$, at a location $i$ can be decomposed into its mean value, $V_i$, and fluctuating component $v_i(t)$, as follows:

$$\tilde{V}_i(t) = V_i + v_i(t). \quad [2]$$

Here, SNR is defined as the normalized standard deviation of an instantaneous void signal as follows:

$$\text{SNR} = \frac{\sigma_{\tilde{V}_i}}{V_i}, \quad [3]$$

where $\sigma_{\tilde{V}_i}$ is the standard deviation of the instantaneous void signal. The normalized random error of the standard deviation is less than 2.2%.

By applying the fast Fourier transform (FFT) technique to the digitized fluctuating components, the power-spectral density function (PSDF) and auto-correlation function (ACF), as typically shown in figures 4(a) and 5, are estimated from each sensor signal. Two types of flow time scales are determined from the ACFs of the fluctuating and instantaneous void signals.

A time scale, $T_f$, is evaluated to relate it to the developing mode of the bubble flow structures. It is defined, as typically shown in figure 5, as the time at which the magnitude of the ACF, evaluated from a fluctuating signal, is half its maximum, and indicates the measure of time duration within which the identity of the flow structures is maintained as propagating. Another time scale, $T_m$, which will be used as an indicator of BSFRT, is defined as the time at which the magnitude of the ACF, evaluated from an instantaneous signal, is half its maximum.

For a pair of signals from successive void sensors $i, j$, several statistical parameters are estimated to determine the wave propagation properties. They include the cross-spectral density function (CSDF), correlation coefficient function (CCF), transfer function and coherence function (COH). In figure 4 the typical shape of these parameters is shown.

The estimates of CCF, $\hat{\rho}_{ij}(\tau)$, and transfer function, $\hat{H}_{ij}(f)$, are defined as

$$\hat{\rho}_{ij}(\tau) = \frac{\hat{R}_{ij}(\tau)}{\hat{\sigma}_i \hat{\sigma}_j} \quad [4]$$

and

$$\hat{H}_{ij}(f) = \frac{\hat{G}_{ij}(f)}{\hat{G}_{ii}(f)}, \quad [5]$$

respectively, where $\hat{R}_{ij}(\tau)$ is the cross-correlation function, $\hat{\sigma}_k$ is the standard deviation of the void signal from a void sensor $k$, and $\hat{G}_{ii}(f)$ is the estimate of PSDF. The estimate of CSDF, $\hat{G}_{ij}(f)$, can be expressed in terms of its magnitude and phase components as follows:

$$\hat{G}_{ij}(f) = |\hat{G}_{ij}(f)| \exp[-i\hat{\theta}_{ij}(f)], \quad [6]$$

where i is the imaginary number and $|\hat{G}_{ij}(f)|$ is the magnitude of CSDF.

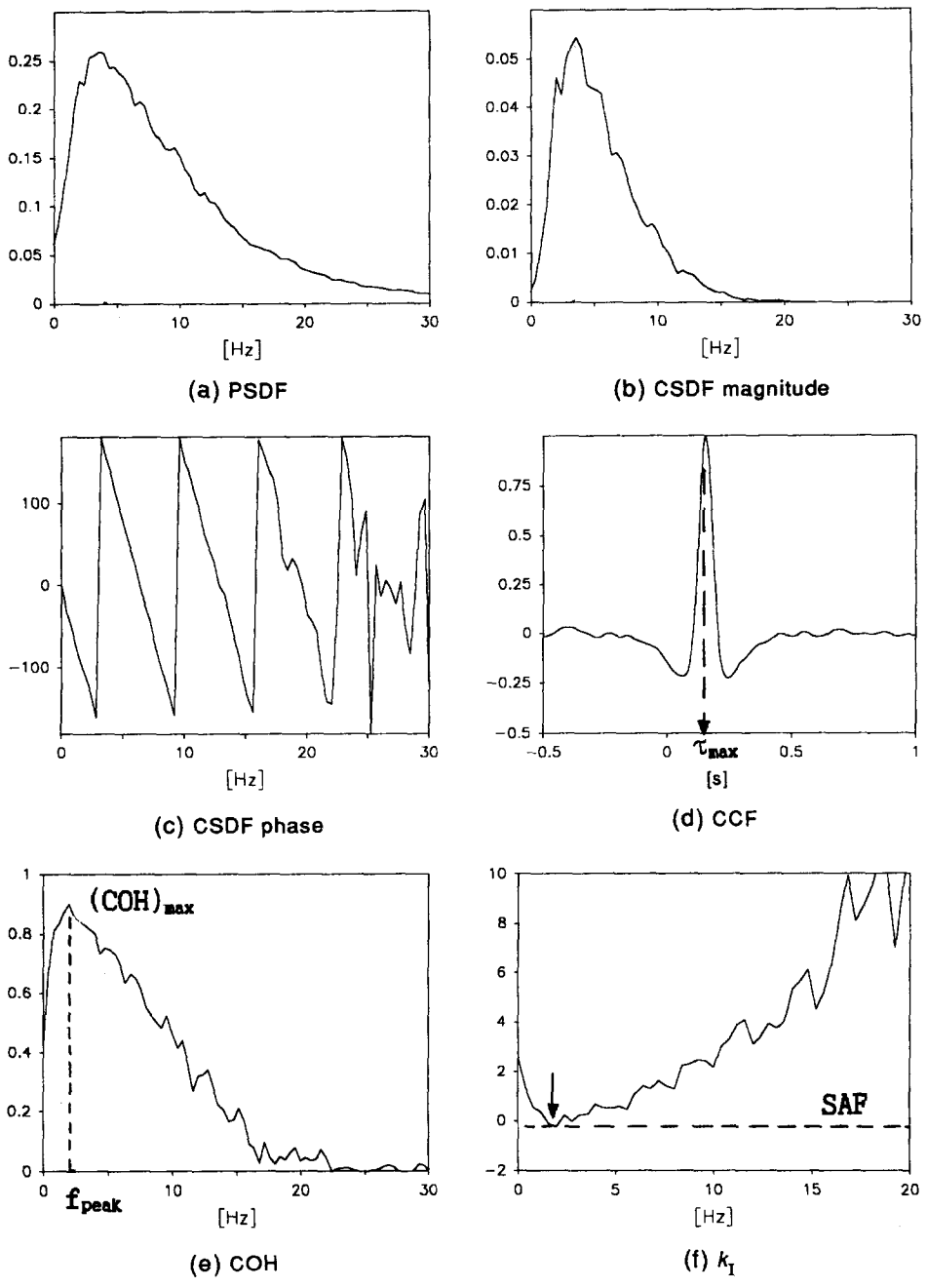


Figure 4. Typical example of the statistical parameters: $J_L = 0.18$ m/s, $\epsilon = 8.6\%$, $D_b = 4.8$ mm. (a) PSDF, (b) CSDF magnitude, (c) CSDF phase, (d) CCF, (e) COH and (f) $k_I$ defined by [9].

The wave propagation speed, $C_\epsilon$, can be estimated as follows:

$$C_\epsilon = \Delta z / \tau_{max}, \qquad [7]$$

where $\Delta z$ is the distance between two successive void sensors, and $\tau_{max}$ can be determined from the slope of the phase factor of CSDF, $\hat{\theta}_{ij}(f)$, as in figure 4(c), or from the peak time of CCF, as shown in figure 4(d). For estimation of the wave speed, CCF is preferable to the cross-correlation function commonly used, in that the former shows a finer peak than the latter and is useful to compare the degree of likeness between the different signals due to their normalized characteristics.

The magnitude of transfer function, $|\hat{H}_{ij}(f)|$, is used to evaluate the degree of spatial attenuations in propagating waves. The fluctuating component of the void signal from sensor $i$ can be described as

$$v_i \sim \exp[\mathrm{i}(kz_i - 2\pi ft)], \quad [8]$$

where $f$ is the frequency and $k$ is the complex wave number which can be decomposed into its real part ($k_R$) and imaginary part ($k_I$). Here, with [5] and [8], the imaginary wave number can be expressed as

$$k_I(f) = -\ln\{|\hat{H}_{ij}(f)|\}/\Delta z. \quad [9]$$

The spatial attenuation factor (SAF) is defined as the minimum value of $k_I$ in the frequency domain, as shown in figure 4(f), since it can be treated as the most unstable factor which will dominantly propagate and be more easily amplified than those with other frequency components.

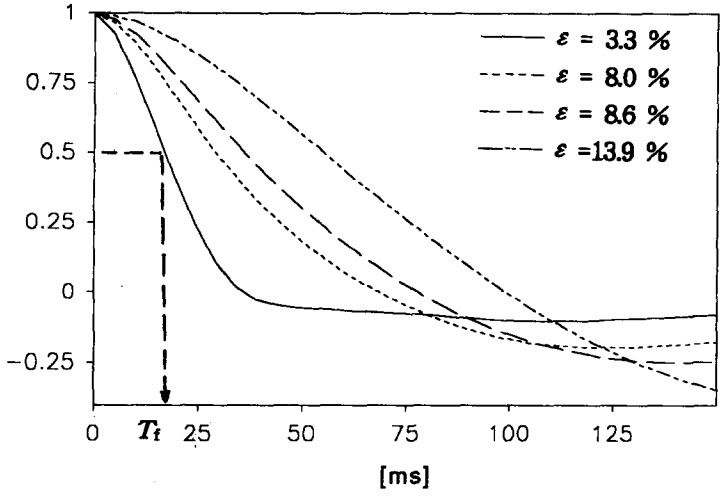


(a) $D_b$ = 4.8 mm

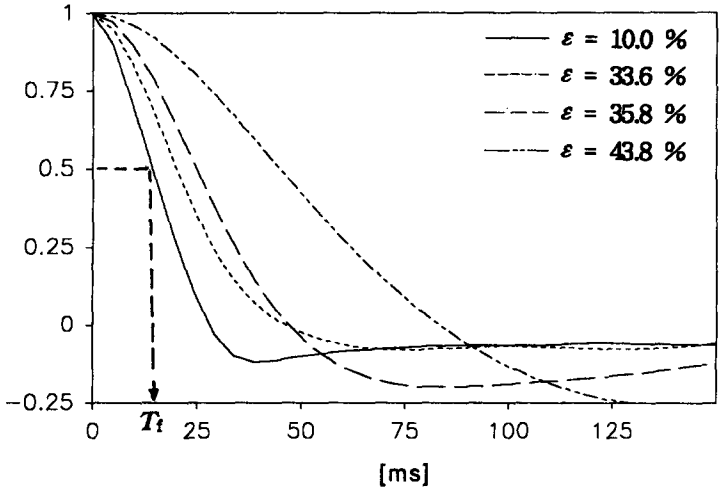


(b) $D_b$ = 2.7 mm

Figure 5. Typical form of the auto-correlation function (ACF): $J_L = 0.18$ m/s. (a) $D = 4.8$ mm and (b) $D_b = 2.7$ mm.

Table 2. Data acquisition/reduction conditions

| Parameters | Value |
|---|---|
| Sampling frequency ($f_s$) | 204.8 Hz |
| Sample record length per channel ($T_r$) | 320 s |
| FFT size ($N_{FFT}$) | 512 |
| Number of ensemble averaging ($N_d$) | 128 |

Actually, the frequency value at which $k_1$ has a minimum is, in most cases, identical to that of the $(COH)_{max}$ at which two signals are mostly correlated. SAF indicates the degree of spatial attenuation/amplification of void fraction waves: a positive value indicates spatial attenuation whereas a negative is spatial amplification, as can be interpreted from [8]. COH is used to evaluate the propagation characteristics of void fraction waves as well as to check the integrity of the measurement system since it indicates the quality of the correlation between two signals.

The data acquisition/reduction conditions are summarized in table 2. The error analysis is performed under these conditions and the results are described in the appendix. The errors in COH, transfer function and phase factor of CSDF are given in table 3 for typical cases. For further details on the definition of estimated parameters and the error evaluations, see Bendat & Piersol (1986).

## 4. RESULTS AND DISCUSSION

### *4.1. Characterization of the flow regime*

For all test runs, four typical flow regimes can be characterized based upon the SNR and PDF of void signals in addition to visual observations as follows:

*(1) Bubbly flow.*

*Discrete bubbly flow:* the gas phase is distributed as discrete bubbles. The time record shows random-like fluctuations with small amplitude and the PDF plot shows a single peak with a narrow width. It appears at a very low void fraction for a large bubble size and over a broad range of void fraction for a small bubble size as shown in figures 6(a) and 7(a)–(c), respectively.

*Clustered bubbly flow:* this flow consists of the bubble clusters, flowing in the center of flow channel, and the discrete bubbles flowing near the channel wall and between the bubble clusters. Bubbly flow with a large bubble size forms bubble clusters even at a low void fraction. Bubble clusters become larger and the bubbles in the clusters coalesce with each other to form cap bubbles while passing through the channel. The bubble clusters are well indicated in the time record by the void fluctuations with large amplitude, and the PDF plot also shows a single peak but with a tail, which shows their passage, as shown in figure 6(b) and (c).

*(2) Churn-type flow.* This appears at a high void fraction with small bubble size not only in the entrance region but also in the upper part of the flow channel. The bubbly flow with a small bubble size continues to appear as the discrete bubbly flow, without clustering, over the entire flow channel with the increase of bubble populations as the gas superficial velocity ($J_G$) increases. At a certain gas flow, the highly packed bubbles suddenly form large and distorted structures of the gas phase which are then developed into Taylor bubbles. This type of flow regime is similar to that defined as "churn flow" by Taitel *et al.* (1980), a form of developing slug flow observed by Mao & Dukler (1993) and that defined as "churn flow of the second kind" by Hewitt & Jayanti (1993), where confusions on the definition of churn flow were clarified. It shows the irregular passage of large

Table 3. Evaluated errors for typical cases

| COH | 0.7 | 0.8 | 0.9 |
|---|---|---|---|
| $U$† (COH) | 8.9% | 6.2% | 2.6% |
| $\epsilon$ ($\|H_{ij}\|$) | 4.1% | 3.1% | 2.1% |
| $U$ ($\theta_{ij}$) | 4.7° | 3.6° | 2.4° |

†$U$ = overall uncertainty; $\epsilon$ = random error.

structures of the gas phase in time record and also shows PDF with two peaks. It is similar to that of slug flow, but the intermediate void region in PDF is not clear when compared to slug flow.

*(3) Slug flow.* The clustered bubbly flow, which appears in the condition of large initial bubble size, is gradually developed into slug flow as $J_G$ increases, whereas churn-type flow, which can form with a small bubble size, is suddenly developed into slug flow by a small addition of gas flow. The PDF plot shows well-defined bimodal shapes as seen in figures 6(e), (f) and 7(f).

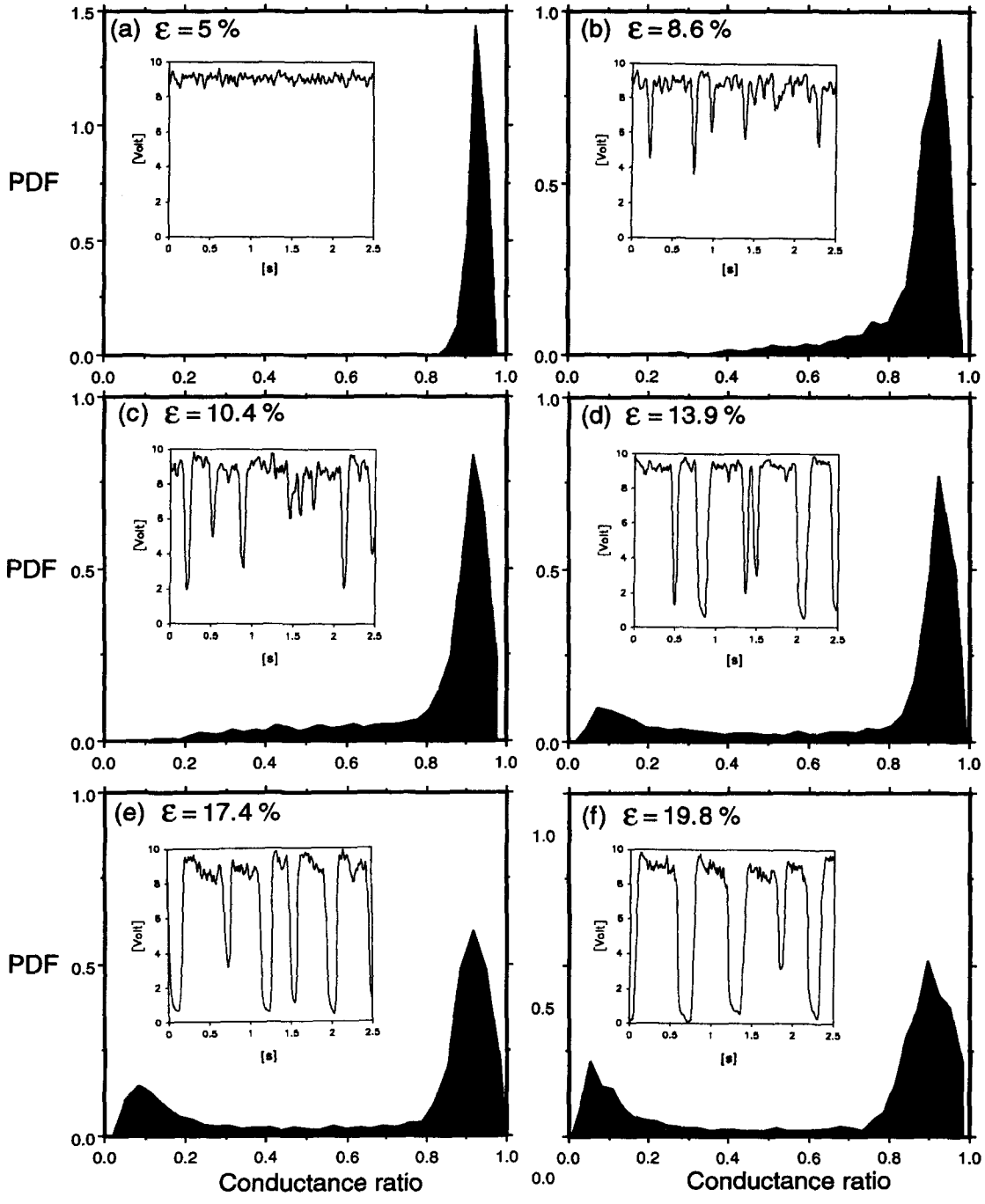


Figure 6. Developments of the bubble flow (I): large bubble case, $D_b = 4.8$ mm, $J_L = 0.18$ m/s. (a) Discrete bubbly flow, $J_G = 0.021$ m/s; (b) clustered bubbly flow, $J_G = 0.042$ m/s; (c) clustered bubbly flow, $J_G = 0.055$ m/s; (d) clustered bubbly flow, $J_G = 0.084$ m/s; (e) slug flow, $J_G = 0.117$ m/s; and (f) slug flow, $J_G = 0.137$ m/s.

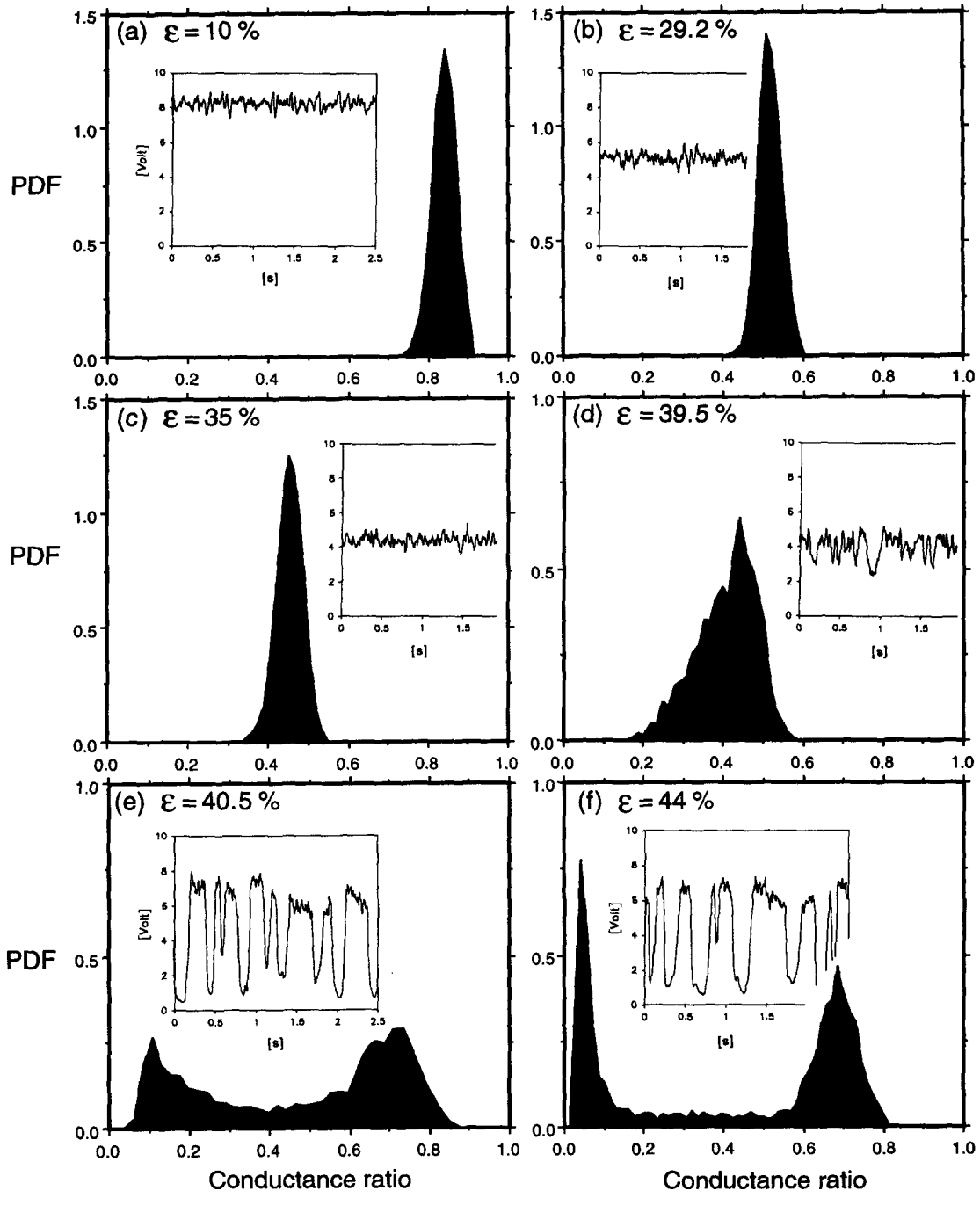


Figure 7. Developments of the bubble flow (II): small bubble case, $D_b = 2.7$ mm, $J_L = 0.275$ m/s. (a) Discrete bubbly flow, $J_G = 0.061$ m/s; (b) discrete bubbly flow, $J_G = 0.212$ m/s; (c) discrete bubbly flow, $J_G = 0.311$ m/s; (d) discrete bubbly flow, $J_G = 0.346$ m/s; (e) slug flow, $J_G = 0.364$ m/s; and (f) slug flow, $J_G = 0.392$ m/s.

The characterization of the flow regimes using the PDF analysis of void signals from the IVM sensor is similar to that of Jones & Zuber (1975) and Kelessidis & Dukler (1989) using X-ray beam attenuation and local conductivity probe signals, respectively. The void signals from the IVM sensor seem, however, to be more practical to use than previous ones since they are representative of the flow information over the entire cross-section of the flow channel.

### 4.2. *Observed flow development*

From the statistical analysis of void signals, it is found that two distinct modes of flow structural developments in bubbly flow are observed, which are dependent on bubble size. The developments of the flow structures are well represented by the time record and PDF, which are typically shown in figures 6 and 7, and by the variation of SNR, as shown in figure 8, for two different modes.

*Large bubble size.* The flow structural developments are illustrated by the time record and the PDF shapes in figure 6 for $J_L = 0.18$ m/s with $D_b = 4.8$ mm. In the case of large bubble size ($D_b = 4.8$, 4.2 mm), the bubble shape is ellipsoidal as presented in table 1, and the radial void profile shows the core peaking at a low void fraction as observed by Serizawa *et al.* (1991) and Liu (1991). As $J_G$ increases, the bubble number density is increased and the bubbles located in the channel center gradually form bubble clusters. Bubbly flow with a large bubble size becomes the clustered bubbly flow with intermittent bubble clusters, as shown in figures 6(b) and (c), when bubbles flow downstream or the gas flow rate is increased. This type of structural development was also observed by Park *et al.* (1993) in a high viscous, low velocity flow condition with uncontrolled bubble sizes.

As bubbles flow downstream or the gas flow rate is increased, the bubbles in the bubble clusters collide and coalesce to form cap bubbles, as seen in figure 6(d). As a result, the rate of agglomeration/coalescence of bubbles gradually increases due to the wakes in the region behind the cap bubbles. This finally results in the gradual transition to slug flow even below $\epsilon = 0.2$, as is well represented by figures 6(e) and (f). It contradicts previous observations such that no Taylor bubble appears along the flow channel for $\epsilon < 0.25$.

The gradual flow developments are well represented by SNR in figure 8 for $D_b = 4.8$ mm at $J_L = 0.18$, 0.275 and 0.49 m/s. The flow structural developments are also well represented by the variation of the time scale, $T_f$, which is plotted versus void fraction in figure 9 for different bubble sizes at $J_L = 0.18$, 0.275 and 0.49 m/s. For the case of $D_b = 4.8$ mm, small values at a low void fraction are indicated, but these increase gradually as the clustering of bubbles continues to form with an increase in gas flow.

At higher liquid flow rates, the tendency of flow structural development is similar to that of a low liquid flow rate, but the bubble clustering and formation of cap bubbles tend to go on over a relatively broader range of void fraction than at low liquid flow rates.

It is observed that the bubbly flow with a large bubble size shows no random collisions between bubbles, but gradual coalescence occurs due to collisions induced by the wakes behind the leading

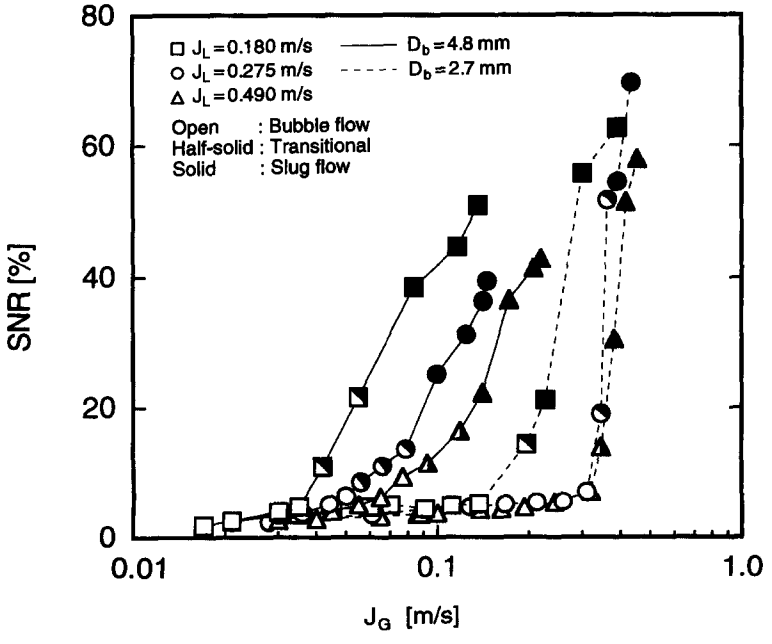


Figure 8. Variation of the signal-to-noise ratio (SNR).

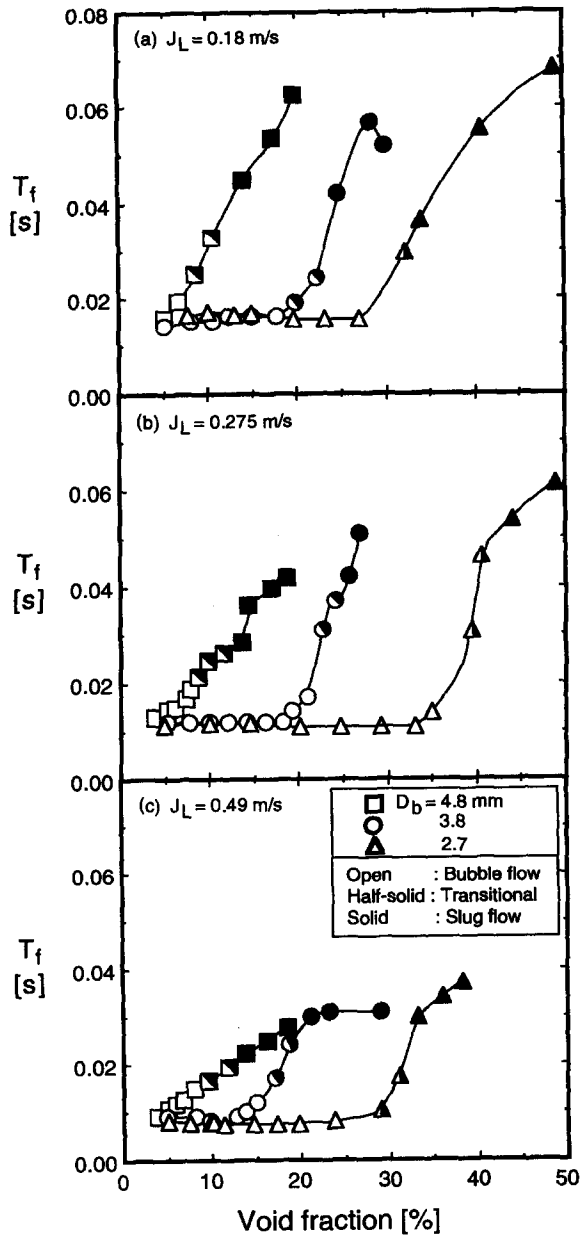


Figure 9. Variation of the apparent time scale, $T_f$. (a) $J_L = 0.18$ m/s, (b) $J_L = 0.275$ m/s and (c) $J_L = 0.49$ m/s.

bubbles or bubble clusters. The collision frequency increases continuously along the flow channel even in fixed gas flow conditions. This requires a relatively long transitional length as observed by Liu (1993).

*Small bubble size.* In bubbly flow with a small bubble size, near-wall peaking of the radial void profile in a low void fraction range is shown, and it is observed that the bubbles tend to be uniformly distributed as the gas flow rate and void fraction increase. The gas phase flows along the flow channel as discrete bubbles without forming bubble clustering, as shown in figure 7(a) and (b), while the bubble number density gradually increases as $J_G$ is increased. With a further increase of $J_G$, the highly packed bubble flow is formed even though the void fraction far exceeds 0.3, as shown in figure 7(c) and (d).

At a certain population of bubbles, abrupt coalescence of the packed bubbles appears to form the large and distorted structures of gas phase which show the characteristics of churn-type flow.

These unstable structures are suddenly developed into Taylor bubbles to form slug flow only by a small addition of gas flow, as in figure 7(e). The critical gas flow rate, at which Taylor bubbles are suddenly formed out of the packed bubbles, depends on $J_L$, and the critical void fraction goes up to about $\epsilon = 0.4$ at $D_b = 2.7$ mm as shown in figure 7(d).

The flow structural developments for small bubble size, including the abrupt changes of flow structures, are well represented by the variation of SNR in figure 8 for $D_b = 2.7$ mm at $J_L = 0.18$, 0.275 and 0.49 m/s and are also represented by variation of the flow time scale, $T_f$, as shown in figure 9 for $D_b = 3.8$ and 2.7 mm at $J_L = 0.18$, 0.275 and 0.49 m/s. For small bubble sizes, the time scale shows small values with little variation over the entire bubbly flow region. Once the large structures of the gas phase appear, however, it increases abruptly.

The bubbly flow with small bubble size shows random collisions without any gradual coalescence, as observed by Qazi *et al.* (1983) (no bubble size is mentioned in their work), while the bubble number density increases continuously as gas flow increases. No bubble clusters nor cap bubbles appear in the process of BSFRT, and the transitional void fraction lies in the range of $\epsilon = 0.20$–$0.4$ depending on the bubble size as well as on the liquid flow rate. There is no appearance of gradual bubble clustering but the sudden formation of Taylor bubbles occurs in all cases of liquid flow considered herein.

The varying tendency of the time scale, $T_f$, well indicates the mode of flow structural developments. $T_f$ can be interpreted as a measure of the *local* time scale, like the relaxation time of the flow: the small value of $T_f$, corresponding to the case of the discrete bubbly flow, indicates that the information representing the local flow structures is lost in a very short time and newly born sources of fluctuations are generated. This can be assured by the fact that the void fluctuations in discrete bubbly flow are very random-like with small amplitudes, as observed from other statistical parameters such as PDF and SNR. The large value of $T_f$, corresponding to transitional and slug flow, indicates that the flow information at an instant is maintained to propagate to some degree for certain durations. It should be noted that the time scale, $T_f$, becomes shorter as liquid flow is increased, as seen in figure 9.

It turns out, from Taitel (1990), that the existence of bubbly flow is almost independent of the gas injection methods, except at the entrance region. Furthermore, from Hewitt (1990), there is no effect of channel length on the transition condition. It is also shown, in Liu (1993) and Qazi *et al.* (1993), that $L/D = 100$ is sufficient for a fully developed flow. Therefore, the behavior of the flow structures observed in the present study would not lose its general applicability.

### *4.3. Wave propagation properties*

*Wave speed.* The wave speeds, determined based upon the peak time of CCF, are compared in figure 10(a) for $J_L = 0.18$ m/s with different bubble sizes. In the large bubble case ($D_b = 4.8$ mm) shows a gradual increase of wave speed with void fraction, which corresponds to the gradual growth of bubble clusters. This trend was also observed by Park *et al.* (1993) at the high viscous, very low velocity conditions without controlling bubble size.

For small bubble sizes, the wave speed is slightly decreased with void fraction in the bubbly flow regime as previously observed, but in transitional and slug flow regimes, it increases very sharply as shown in figure 10(a) for $D_b = 2.7$ and 3.2 mm. The drastic change in wave speed indicates a propagation mode which is different from that of the bubbly flow regime.

For higher liquid flow ($J_L = 0.275$ and 0.49 m/s), as shown in figures 10(b) and (c), the bubbly flow with $D_b = 4.8$ mm shows the same tendency as for $J_L = 0.18$ m/s. However, the bubbly flow with a small bubble size shows the different trends of wave speed. At $J_L = 0.275$ m/s, it is nearly constant, irrespective of the change of void fraction, as can be seen in figure 10(b), but continuously increases with void fraction at $J_L = 0.49$ m/s as in figure 10(c). The varying tendency of wave speed with void fraction in discrete bubbly flow is dependent on the liquid flow rate, which is different from most previous observations (e.g. Matuszkiewicz *et al.* 1987; Saiz-Jabardo & Bouré 1989) such that the wave speed slightly decreases with void fraction in bubbly flow. Once the large structure of gas phase is formed, it increases very sharply as in low liquid flow. The overall uncertainty of the wave speed, $C_c$, is determined to be less than 7.2%.

The wave speed relative to the mixture volumetric flux ($J$) is typically shown in figure 11 for $J_L = 0.18$ and 0.275 m/s. For small bubble sizes, it tends to near-zero as void fraction increases,

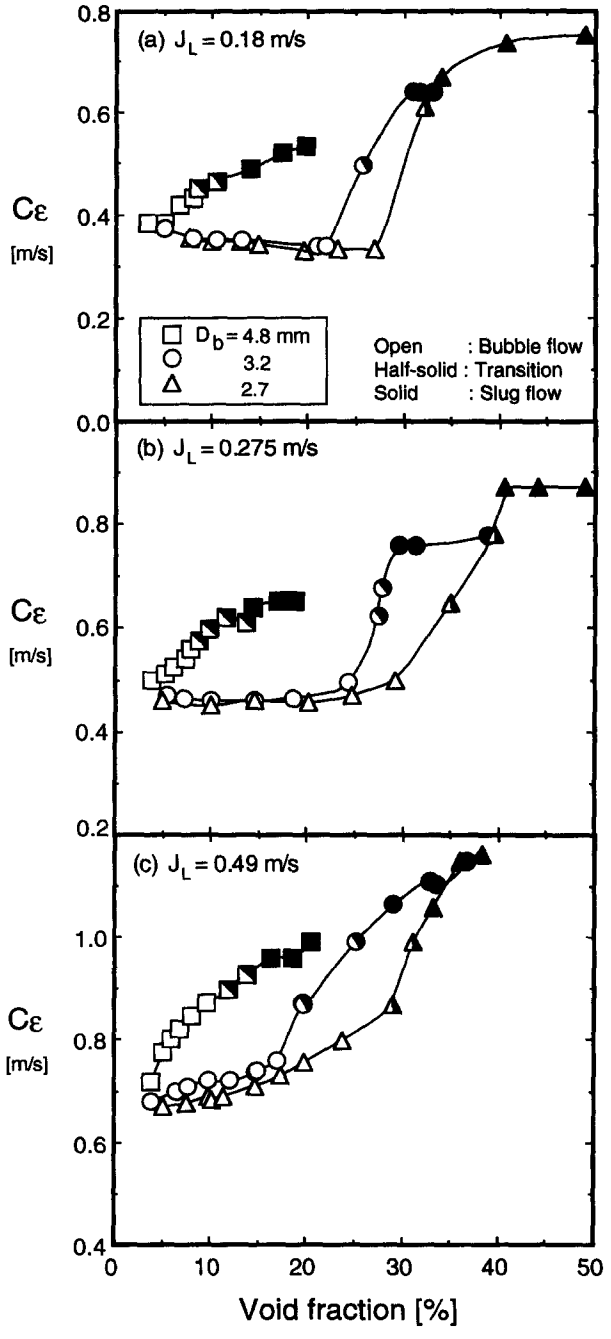


Figure 10. Wave propagation speed. (a) $J_L = 0.18$ m/s, (b) $J_L = 0.275$ m/s and (c) $J_L = 0.49$ m/s.

and this indicates that, in a highly packed bubble flow, the flow information on the two-phase mixtures is transported at the same speed as the mixture volumetric flux.

The wave propagation speed in bubbly flow shows two different types of tendency, depending on the characteristics of the flow development. The wave speed of the clustered bubbly flow, which occurs in the large bubble case, increases gradually with void fraction, and the wave speed relative to mixture volumetric flux is also continuously increasing. In discrete bubbly flow, however, wave speed shows small variations with void fraction and is dependent on the liquid flow rate. Then, it increases abruptly in the transition region.

*Peak frequency and wavelength.* For void fraction waves naturally generated, the determination of a major frequency component which is dominant in the propagation is required to evaluate the characteristics of propagating waves, including the dominant frequency and corresponding wavelength. Here, the wavelength is defined as $\lambda = C_c/f_{peak}$, where the peak frequency ($f_{peak}$) is revealed in the COH diagram as typically shown in figure 4(e), and it can be considered as the dominant frequency component.

As discussed earlier, the bubbly flow with large bubble size is accompanied by bubble clusters during the transition to slug flow, and will show characteristics such that the propagation of the clustered bubbles is dominant. It is observed that the prevailing propagation frequency of the bubble clusters is in the range of $2.8 < f_{peak} < 3.6$ Hz for $J_L = 0.18$ m/s. Slug flow shows a relatively simple and narrow spectrum with $1.6 < f_{peak} < 2.4$ Hz which indicates a wider range of slug frequency than those (around 1.0 Hz) observed by Matuszkiewicz *et al.* (1987) and Jones & Zuber (1975).

As the liquid flow increases and the bubble size decreases, the structure of the spectrum in bubbly flow becomes wider and more complicated, and their peak frequency tends to increase. The spectrum observed in these cases shows a wider range of frequency than previous observations of a few hertz.

The wavelength is evaluated from the peak frequency of COH which represents the most coherent frequency component for two different signals. For the large bubble case, it shows linearly increasing trends with void fraction in the range of $\lambda = 0.15$–$0.4$ m as can be seen in figure 12(a).

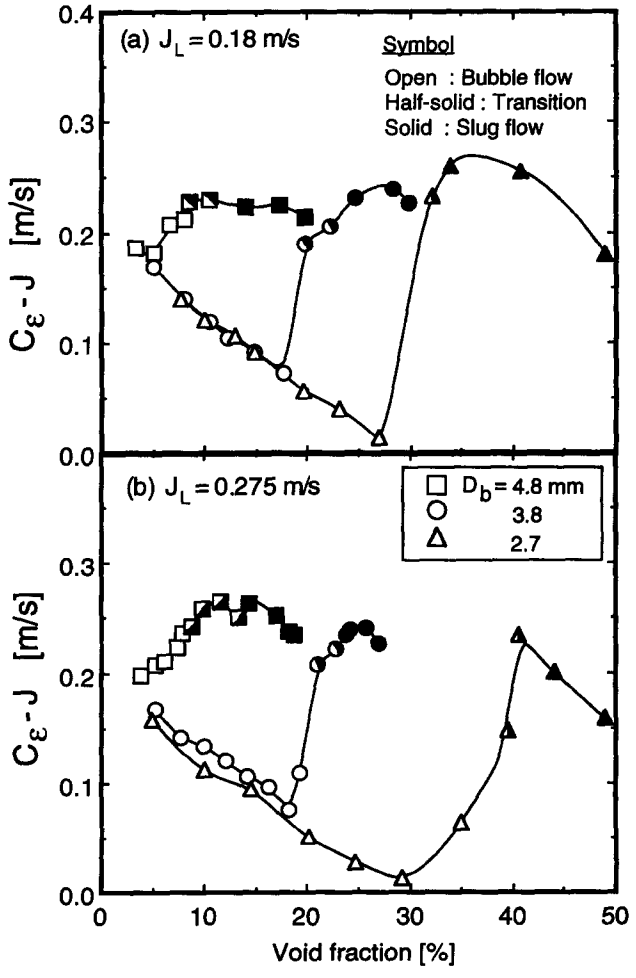


Figure 11. Wave speed relative to the mixture volumetric flux. (a) $J_L = 0.18$ m/s and (b) $J_L = 0.275$ m/s.

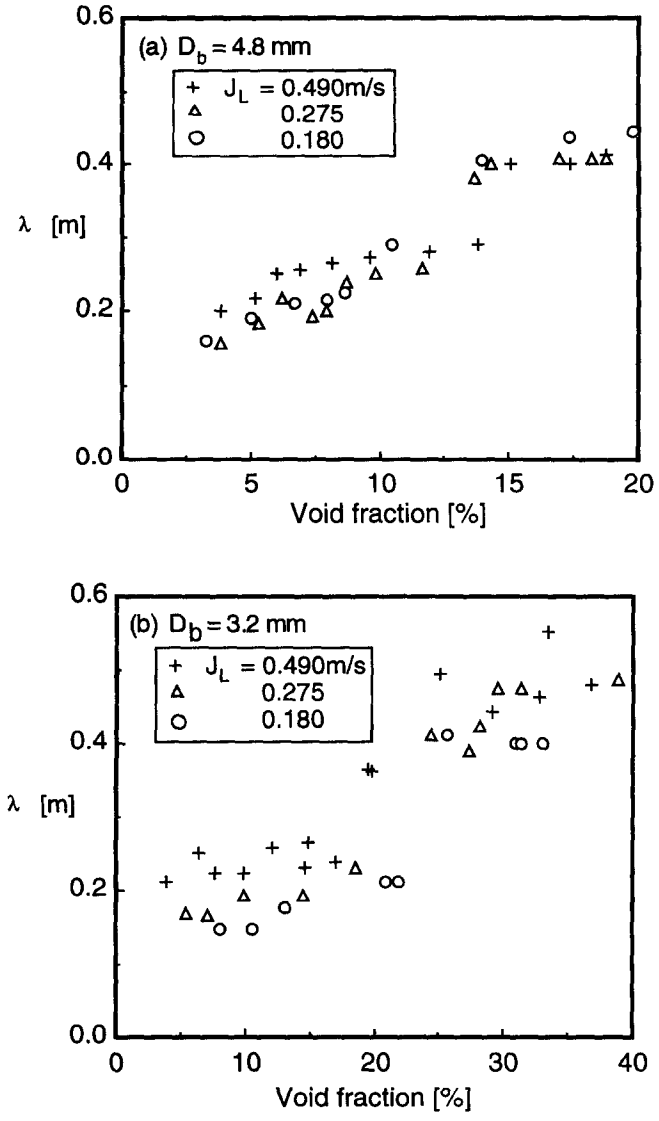


Figure 12. Distribution of the wavelength. (a) $D_b = 4.8$ mm and (b) $D_b = 3.2$ mm.

The small bubble size case, as typically shown in figure 12(b) for $D_b = 3.2$ mm, shows trends which are different from the case of large bubble size. In discrete bubbly flow, it does not deviate much around $\lambda = 0.2$ m, which is much smaller than that (about 0.3 m) observed by Matuszkiewicz *et al.* (1987) where the width of a void sensor is about three times larger than the present study. However, it increases sharply in the transition region and reaches 0.5 m in the slug flow region. The variation of wavelength reveals well the characteristics of the developing flow structures.

*Wave instability.* The degree of the spatial amplification/attenuation of the void fraction waves is quantified in terms of SAF. The variation of SAF with void fraction is shown in figure 13 for different conditions of liquid velocity and bubble size.

For the large bubble case ($D_b = 4.8$ and 4.2 mm), SAF decreases gradually with void fraction. The bubbly flow with clustering indicates the near-zero value of SAF, where the bubble clusters are formed and then grow. Then, the gradual growth of bubble clusters to form cap bubbles is indicated by a negative SAF indicating wave amplification. This tendency is the same as that observed by Park *et al.* (1993) at high viscous, very low flow conditions. The transitional flow regime, which includes the growth of bubble clusters and the formation of cap bubbles, exists over a broader range of void fraction as $J_L$ increases. This may be attributed to the turbulence breakup effect which is expected to increase with the liquid flow rate.

The small bubble size case (e.g. $D_b = 2.7$ and 3.2 mm) shows that the varying tendency of SAF is very different from the large bubble case. The void waves are strongly attenuated over a broad range of void fraction in the bubbly flow region, and the attenuation tends to increase as the bubbles become highly packed as shown in figure 13(a) for $J_L = 0.12$ m/s. This could be explained by the observation that, as the void fraction increases, the packed bubbles flow in a random-like manner with smaller amplitude of fluctuations, but without any gradual coalescence. SAF decreases sharply near a certain void fraction, and it tends to near-zero or a slightly negative value which corresponds to the initiation of churn-type flow. As $J_G$ increases beyond this critical value, the transition flow grows very quickly to form slug flow where SAF changes its sign to the negative and the propagating waves are amplified. It is interesting to note that the waves tend to become re-stabilized as the slug flow is developed.

For $J_L = 0.18$, 0.275 and 0.49 m/s, very similar tendencies to that for $J_L = 0.12$ m/s are observed. For the small bubble size case, therefore, the initiation of spatial amplification corresponds to the transition from bubbly flow to slug flow.

A time scale, $T_m$, can be also used to relate it with the structural developments. In figure 14, $T_m$ is plotted versus void fraction for typical bubble sizes ($D_b = 2.7$, 3.8 and 4.8 mm) at $J_L = 0.18$, 0.275 and 0.49 m/s. The first falling-off point of $T_m$ indicates quite well the appearance of the large structures of the gas phase, which can be determined from the variation of PDF, SNR and $T_f$. $T_m$ can be interpreted to be associated with a *global* time scale representing the behavior of apparent

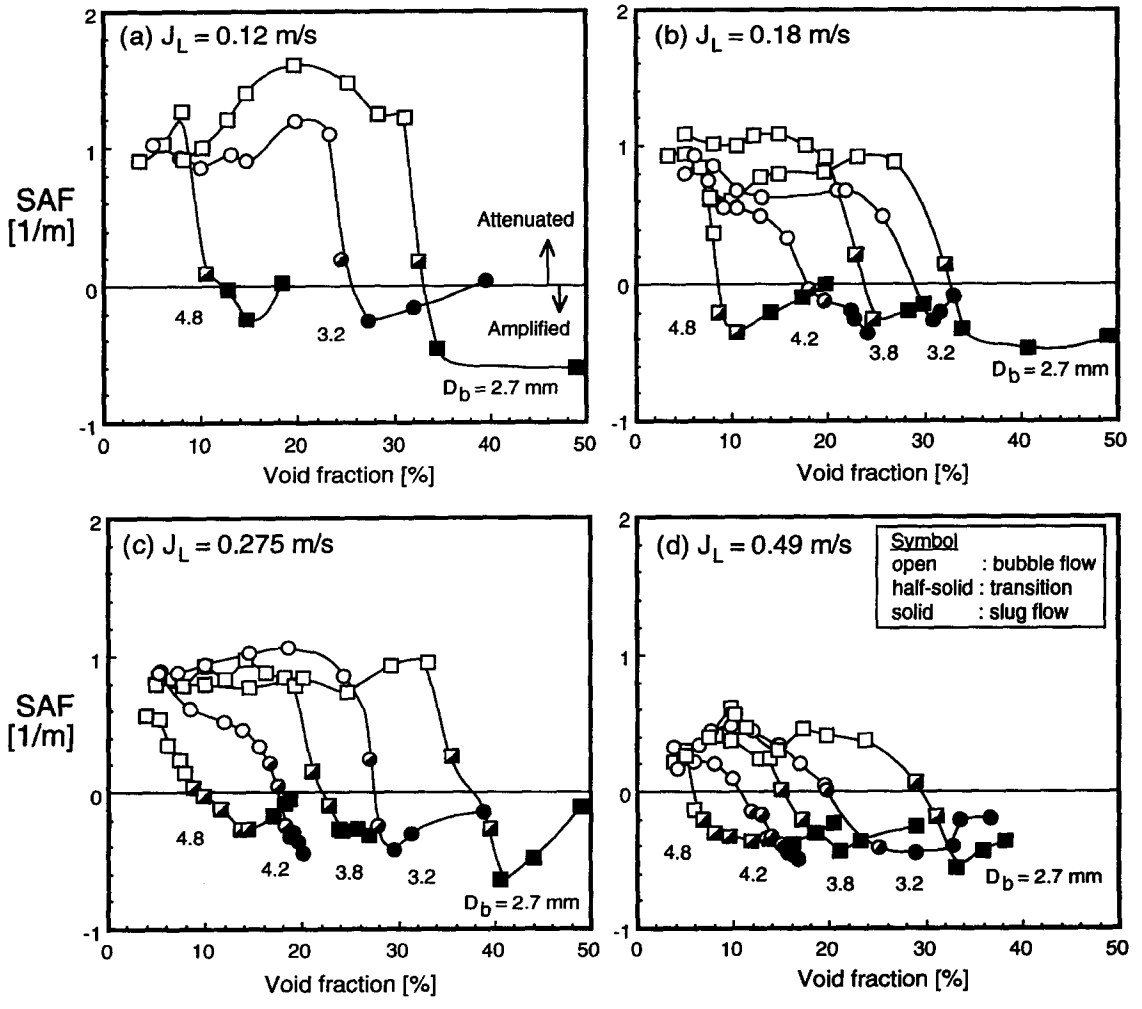


Figure 13. Variation of the spatial attenuation factor. (a) $J_L = 0.12$ m/s, (b) $J_L = 0.18$ m/s, (c) $J_L = 0.275$ m/s and (d) $J_L = 0.49$ m/s.

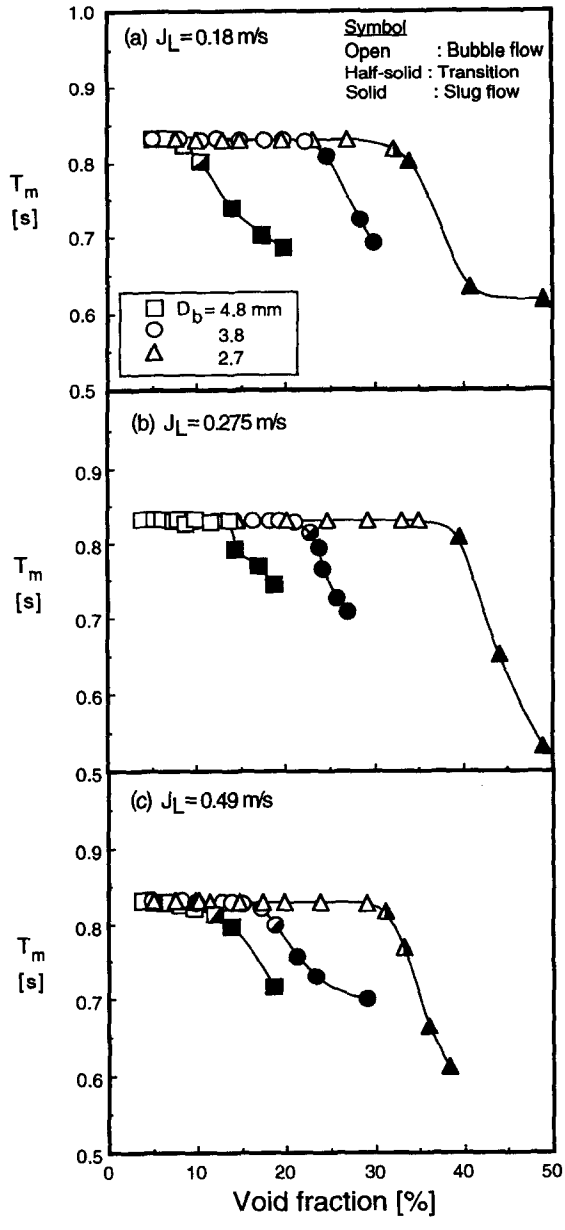


Figure 14. Variation of the apparent time scale, $T_m$. (a) $J_L = 0.18$ m/s, (b) $J_L = 0.275$ m/s and (c) $J_L = 0.49$ m/s.

flow structures since it is estimated from the instantaneous void signals which contain the global information of the flow including both the mean void fraction and void fluctuations.

Most previous investigators have observed that the void fraction waves are attenuated for bubbly flow but their attenuation decreases as the mean void fraction increases, and that BSFRT occurs gradually over a broad range of void fraction. When compared to the present observations, where the varying tendency of wave damping with void fraction is dependent upon the developing mode of flow structures which are sensitive to bubble size, it can be said that previous observations came from the experiments without separating the bubble size effect from the others. As a result, the previous observations of the tendency of decreasing wave damping with void fraction and a smooth transitional process would be mainly due to the gradual increase of the initial bubble size, as gas flow increases, and partly due to the hydrostatic head effect on the bubble growth.

The attenuation characteristics of propagating void waves are closely related to the flow structural developments, and an increase in liquid flow rates generally reduces the wave attenuation. The initiation of the instability of void fraction waves basically means that the coalescences of bubbles begin to form the large structures of gas phase. In bubbly flow with large bubble size, it indicates the development of bubble clustering to form cap bubbles, whereas, in bubbly flow with small bubble size, it means the appearance of Taylor bubbles. Therefore, the neutral stability condition (SAF = 0) of void fraction waves can be used as a tool of BSFRT indicator. And it can be supplemented by the time scale, $T_m$.

*Coherence function.* The variation of COH, whose values are chosen at the peak frequency, is closely related to the attenuation characteristics of propagating void waves. The COH variation with void fraction is tabulated in table 4 typically for $J_L = 0.275$ m/s with $D_b = 2.7$, 3.8 and 4.8 mm.

In bubbly flow with small bubble sizes, COH decreases as void fraction is increased to the highly packed bubble flow conditions where the propagating waves are much attenuated. In this case, it can be conjectured that the void signals between the successive void sensors are weakly correlated to the observation that the void fluctuations are very random-like with small amplitude. Once the large structures of gas phase appears, however, it flows with some periodicity and larger amplitude of fluctuations than highly populated discrete bubbles. Thus, COH increases and its maximum value is around 0.95–0.98 in slug flow where the void fluctuations have a very large amplitude with high periodicity due to the rather regular passages of Taylor bubbles. These varying tendencies are well represented for $D_b = 2.7$ and 3.8 mm in table 4(b) and (c). The sharp change in the COH values was also observed near the transition region by Matuszkiewics *et al.* (1987) in the fixed flow condition of $J_L = 0.18$ m/s.

Unlike bubbly flow with small bubble sizes, bubbly flow with large bubble sizes shows a relatively higher value of COH even in the bubbly flow region since it contains clustered bubbles which flow somewhat regularly even at a low void fraction and the bubble clustering increases with void fraction. These are well represented for $D_b = 4.8$ mm in table 4(a).

The variation of COH with void fraction is closely associated to the developing mode of flow structures and well indicates the attenuation characteristics of propagating void waves. Saiz-Jabardo & Bouré (1989) showed the relation of COH with wave attenuation in connection with axial flow developments under fixed flow conditions.

### 4.4. *Bubble size effect on BSFRT*

As discussed above, it is evident that the bubble size and its effect on the behavior of the interactions between bubbles and the surrounding liquid could cause the variation of local flow structures and eventually influence the appearance of global flow structures, that is, BSFRT. Before

Table 4. Variation of the COH values ($J_L = 0.275$ m/s)

| (a) $D_b = 4.8$ mm | | | (b) $D_b = 3.8$ mm | | | (c) $D_b = 2.7$ mm | | |
|---|---|---|---|---|---|---|---|---|
| Void (%) | COH | Flow† regime | Void (%) | COH | Flow regime | Void (%) | COH | Flow regime |
| 3.8 | 0.76 | DB | 5.2 | 0.68 | DB | 5.0 | 0.71 | DB |
| 5.3 | 0.80 | DB | 7.7 | 0.72 | DB | 10.0 | 0.73 | DB |
| 6.2 | 0.83 | DB | 10.0 | 0.72 | DB | 14.4 | 0.74 | DB |
| 7.4 | 0.84 | DB | 12.0 | 0.70 | DB | 20.0 | 0.69 | DB |
| 7.9 | 0.85 | DB | 14.2 | 0.71 | DB | 24.6 | 0.72 | DB |
| 8.7 | 0.90 | CB | 16.2 | 0.69 | DB | 29.2 | 0.67 | DB |
| 9.8 | 0.91 | CB | 18.1 | 0.69 | DB | 33.0 | 0.66 | DB |
| 11.6 | 0.91 | CB | 19.2 | 0.65 | DB | 35.0 | 0.77 | DB |
| 13.6 | 0.91 | CB | 20.9 | 0.84 | (C) B | 39.5 | 0.94 | (C) B |
| 14.3 | 0.94 | SG | 22.7 | 0.91 | (C) B | 40.5 | 0.97 | CH |
| 16.9 | 0.96 | SG | 24.2 | 0.95 | CH | 44.0 | 0.97 | SG |
| 18.2 | 0.96 | SG | 25.7 | 0.97 | SG | 49.0 | 0.98 | SG |
| 18.7 | 0.96 | SG | 27.0 | 0.97 | SG | | | |

†DB = discrete bubbly flow; CB = clustered bubbly flow; CH = churn-type flow; SG = slug flow.

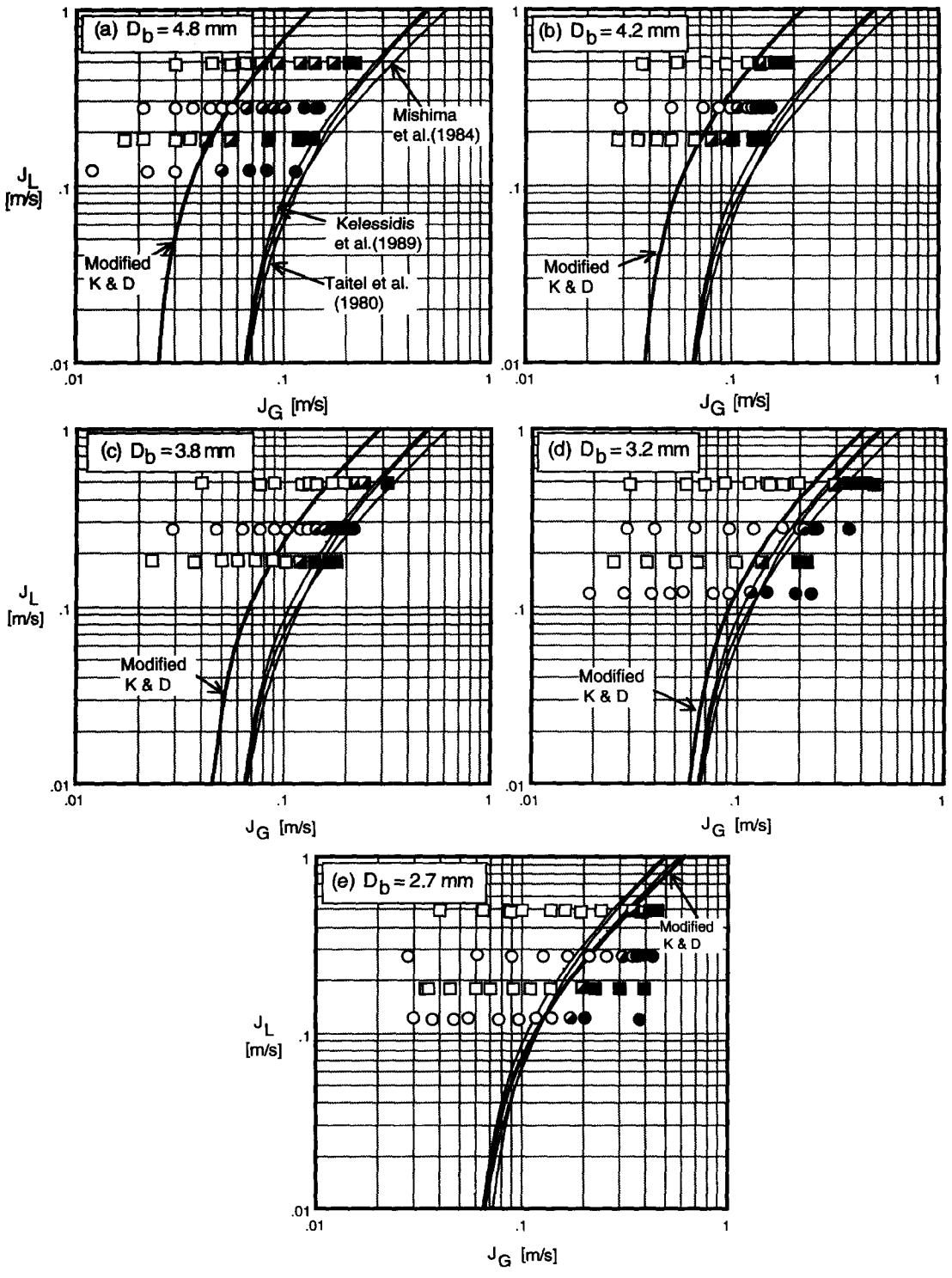


Figure 15. BSFRT boundary: bubble size effect. (a) $D_b = 4.8$ mm, (b) $D_b = 4.2$ mm, (c) $D_b = 3.8$ mm, (d) $D_b = 3.2$ mm and (e) $D_b = 2.7$ mm.

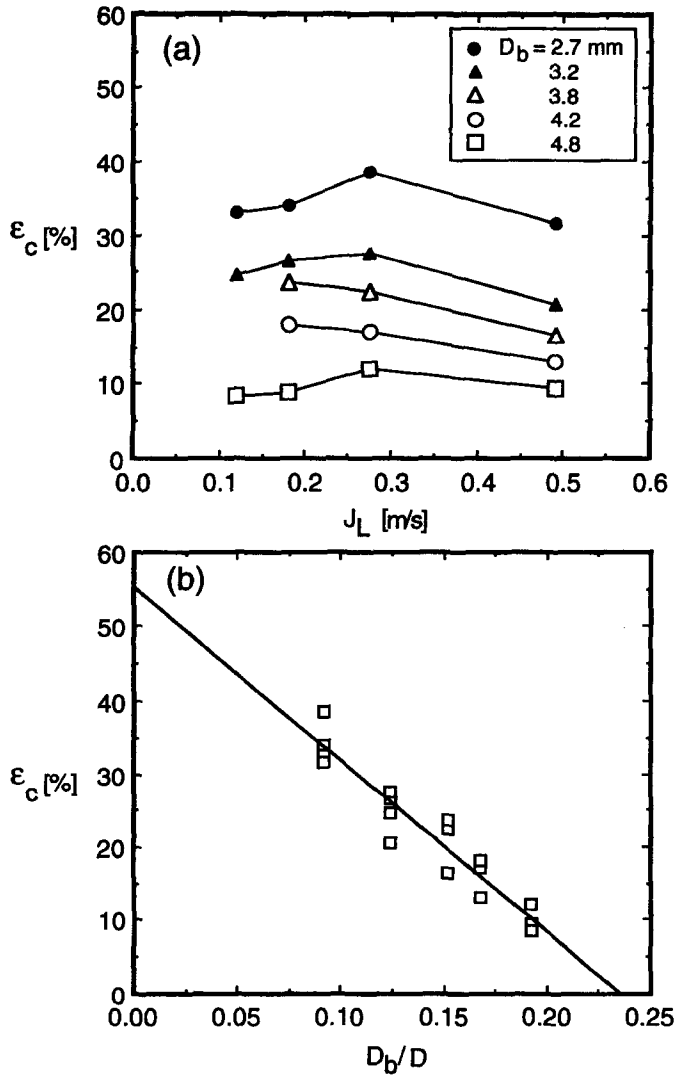


Figure 16. Variation of the critical void fraction, $\epsilon_c$. (a) Critical void fraction vs $J_L$ and (b) critical void fraction vs $D_b/D$.

further discussing the bubble size effect on BSFRT, the existing criteria for BSFRT are briefly reviewed.

Models frequently used for the BSFRT criteria include Taitel *et al.* (1980) and Mishima & Ishii (1984) who assumed that BSFRT occurs at $\epsilon = 0.25$ and 0.3, respectively. Taitel *et al.* (1980) modeled the BSFRT criterion as follows:

$$J_L = 3.0J_G - 1.15\left[\frac{\sigma g(\rho_L - \rho_G)}{\rho_L^2}\right]^{1/4}. \quad [10]$$

Mishima & Ishii (1984) derived the following criterion:

$$J_L = \left(\frac{3.33}{C_0} - 1\right)J_G - \frac{0.76}{C_0}\left[\frac{\sigma g(\rho_L - \rho_G)}{\rho_L^2}\right]^{1/4}, \quad [11]$$

where the distribution parameter, $C_0$, is defined as

$$C_0 = 1.2 - 0.2\sqrt{\rho_G/\rho_L}.$$

Kelessidis & Dukler (1989) derived the criterion from the simple analysis as follows:

$$J_L = J_G\left(\frac{1-\epsilon}{\epsilon}\right) - 1.53(1-\epsilon)^{3/2}\left[\frac{\sigma g(\rho_L - \rho_G)}{\rho_L^2}\right]^{1/4}, \quad [12a]$$

and this becomes

$$J_L = 3.0J_G - \left[\frac{\sigma g(\rho_L - \rho_G)}{\rho_L^2}\right]^{1/4} \quad [12b]$$

by letting $\epsilon = 0.25$ at BSFRT.

In figure 15, the flow regime of each experimental data point is represented in the $J_L$–$J_G$ plane for each size of bubble. The BSFRT criteria expressed by [10], [11] and [12b] are also compared. For the large bubble case ($D_b = 4.8$ and 4.2 mm), BSFRT occurs at a smaller gas flow than predicted by existing models, whereas, the case of intermediate bubble sizes ($D_b = 3.8$ and 3.2 mm) is relatively well represented by the models. For a small bubble size ($D_b = 2.7$ mm), however, BSFRT occurs at a larger gas flow than predicted by the models.

The critical void fraction, $\epsilon_c$, which indicates BSFRT, is very dependent on bubble size even under the fixed liquid flow rate, as shown in figure 16(a). In figure 16(b), the critical void fraction is plotted versus bubble size, and the fitted curve can be expressed by

$$\epsilon_c = 0.55 - 2.37\left(\frac{D_b}{D}\right), \quad [13]$$

where $D$ is the inside diameter of the flow channel. It is interesting to note that the critical void fraction, limiting the bubble size to zero, is close to the maximum allowable bubble density, 0.52, which is valid if one assumes that the bubbles are spherical and arranged in a cubic lattice (Taitel *et al.* 1980).

The BSFRT criterion expressed by [12a] with [13] instead of $\epsilon = 0.25$ or 0.3 is also compared with the experimental data in figure 15. The experimental BSFRT boundary is well represented by this criterion. Physical models for BSFRT criteria, therefore, should consider the bubble size and its effect on the behavior of bubble interactions, the developing modes of flow structures and the mechanisms to govern the slug formation.

## 5. SUMMARY AND CONCLUSIONS

The behavior of structural developments in bubbly flow and their effect on the propagation properties of naturally occurring void fraction waves are investigated by systematically varying the bubble size over a wide range of flow conditions in a vertically upwards, air–water flow.

The developing flow structures are objectively identified by the statistical properties of void signals, including PDF, SNR and the apparent time scales of the two-phase flow. Two distinct modes of structural developments in bubbly flow are observed, which are dependent on the bubble size; and the mechanism of slug formation and the critical void fraction, at which the large structures of the gas phase begin to form, are also much dependent on the bubble size.

The varying tendency of the wave propagating properties, including the wave speed, wavelength and wave damping is closely related to the developing mode of flow structures. Newly observed phenomena on the propagation properties of void fraction waves are also presented; and it is evident that the different features of the wave propagation properties are mainly due to the differences in the developing mode of the flow structures.

The wave attenuation phenomena can be well quantified by the spatial attenuation factor (SAF). The wave attenuation is closely associated with the flow structural developments, and it is generally reduced by increasing the liquid flow rate. The neutral stability condition indicates exactly the appearance of the large structures of the gas phase. So, the spatial attenuation factor can be used as an objective tool to identify the bubble-to-slug flow regime transition, and it can be supplemented by the apparent time scale of the flow.

The bubble size effect on the behavior of the interactions between the phases could cause variation of the flow structural developments, and eventually influences the flow regime transition even though the detailed effect of bubble size is still not clear due to the complicated momentum

interactions. The experimental works and physical models on the phenomena of bubble flow structures, therefore, should be developed to take into account the bubble size effect, or separate it from other effects.

## REFERENCES

BENDAT, J. S. & PIERSOL, A. G. 1986 *Random Data: Analysis and Measurement Procedures*, 2nd edn. Wiley, New York.

BOURÉ, J. A. 1988 Properties of kinematic waves in two-phase pipe flows; consequences on the modeling strategy. Presented at the *European Two-phase Flow Group Meeting*, Brussels, Belgium.

DELHAYE, J. M. FAVREAU, C., SAIZ-JABARDO, J. M. & TOURNAIRE, A. 1987 Experimental investigation on the performance of impedance sensors of two and six electrodes for area averaged void fraction measurements. In *Proc. 24th National Heat Transfer Conf.*, Pittsburgh, PA, pp. 234–239.

HEWITT, G. F. 1990 Non-equilibrium two-phase flow. In *Proc. Heat Transfer '90*, paper No. KN-25, Israel, pp. 385–394.

HEWITT, G. F. & JAYANTI, S. 1993 To churn or not to churn. *Int. J. Multiphase Flow* **19,** 527–529.

JONES, O. C. & ZUBER, N. 1975 The interrelation between void fraction fluctuations and flow patterns in two-phase flow. *Int. J. Multiphase Flow* **2,** 273–306.

KELESSIDIS, V. C. & DUKLER, A. E. 1989 Modelling flow pattern transitions for upward gas–liquid flow in vertical concentric and eccentric annuli. *Int. J. Multiphase Flow* **15,** 173–191.

Kytömaa, H. K. & BRENNEN, C. E. 1991 Small amplitude kinematic wave propagation in two-components media. *Int. J. Multiphase Flow* **17,** 13–26.

LIU, T. J. 1991 The effect of bubble size on void fraction distribution in a vertical channel. In *Proc. Int. Conf. on Multiphase Flows '91*, Tsukuba, Japan, pp. 453–457.

LIU, T. J. 1993 Bubble size and entrance length effects on void development in a vertical channel. *Int. J. Multiphase Flow* **19,** 99–113.

MAO, Z. S. & DUKLER, A. E. 1993 The myth of churn flow? *Int. J. Multiphase Flow* **19,** 377–383.

MATUSZKIEWICZ, A., FLAMAND, J. C. & BOURÉ, J. A. 1987 The bubbly–slug flow pattern transitions and instabilities of void fraction waves. *Int. J. Multiphase Flow* **13,** 199–217.

MISHIMA, K. & ISHII, M. 1984 Flow regime transition criteria for upward two-phase flow in vertical tubes. *Int. J. Heat Mass Transfer* **27,** 723–734.

PARK, J. W., LAHEY, R. T. JR & DREW, D. A. 1993 The measurement of void waves in bubbly two-phase flows. In *Proc. NURETH-6*, Grenoble, 5–8 October, pp. 655–662.

QAZI, M. K., GUIDO LAVALLE, G. & CLAUSSE, A. 1933 Axial development of void fraction profiles in vertical two-phase flow. *Int. J. Multiphase Flow* **19,** 385–389.

SAIZ-JABARDO, J. M. & BOURÉ, J. A. 1989 Experiments on void fraction waves. *Int. J. Multiphase Flow* **15,** 483–493.

SERIZAWA, A., KATAOKA, I., GOFUKU, A., TAKAHASHI, O. & KAWARE, Z. 1991 Effect of initial bubble size on bubbly flow structure. In *Proc. Int. Conf. on Multiphase Flows '91*, Tsukuba, Japan, pp. 547–550.

SNELL, C. C., DECHENE, R. L. & NEWTON, R. E. 1979 Evaluation of a unique void fraction monitoring system. EPRI Report NP-1012.

TAITEL, Y. 1990 Flow pattern transitions in two-phase flow. In *Proc. Heat Transfer '90*, paper No. KN-14, Israel, pp. 237–254.

TAITEL, Y., BARNEA, D. & DUKLER, A. E. 1980 Modelling flow pattern transitions for steady upward gas–liquid flow in vertical tubes. *AIChE Jl* **26,** 345–354.

TOURNAIRE, A. 1987 Détection et Etude des Ondes de Taux de Vide en Ecoulements Diphasique à Bulles jusqu'à la Transition Bulles-Bouchons. Ph.D. thesis, Université Scientifique et Médicale et Institute National Polytechnique de Grenoble, France.

TURNER, J. C. R. 1976 The electrical conductance of liquid fluidized beds of spheres. *Chem. Engng Sci.* **31,** 487–492.

## APPENDIX

### *Errors in Estimated Parameters*

Since only the estimates of the statistical parameters of interest can be obtained from a finite length of samples, the accuracy of parameter estimates should be evaluated. Here, the random error

due to the finite length of the sample records and the bias or fixed error that occurred in the process of data sampling will be evaluated, for an unfavorable case of $\hat{\gamma}_{ij}^2 = 0.7$, with the data acquisition/reduction conditions summarized in table 1. The error analysis is performed based on the ANSI/ASME Performance Test Codes (1985),† and chapters 8 and 9 of Bendat & Piersol (1986).

Normalized random error of PSDF, $\hat{G}_{ii}(f)$, is

$$\epsilon_r[\hat{G}_{ii}(f)] = 1/\sqrt{N_d} \doteq 1/\sqrt{B_e T_r} = 0.088, \quad [A1]$$

where $B_e$ is the resolution bandwidth (Hz) which is equivalent to the frequency of the resolution, $\Delta f$ (=0.2 Hz in this study).

The bias error of COH, $\hat{\gamma}_{ij}^2$, is

$$b[\hat{\gamma}_{ij}^2] \doteq (1 - \hat{\gamma}_{ij}^2)^2/N_d = 0.0007, \quad [A2]$$

where $i$ and $j$ correspond to two simultaneously measured void signals, and the random error of COH is

$$\epsilon[\hat{\gamma}_{ij}^2] = \mathrm{SD}[\hat{\gamma}_{ij}^2]/\gamma_{ij}^2$$

$$\doteq \sqrt{2(1 - \hat{\gamma}_{ij}^2)}/|\hat{\gamma}_{ij}|\sqrt{N_d} = 0.045, \quad [A3]$$

where $|\hat{\gamma}_{ij}|$ and $\mathrm{SD}[\hat{\gamma}_{ij}^2]$ are the positive square root and the standard deviation of COH, respectively. With the 95% confidence level for the true value of COH, the uncertainty estimate will be 8.9% and the interval

$$\gamma_{ij}^2 = 0.7 \pm 0.06$$

represents a band within which the true value of COH is expected to lie. The overall uncertainty for other values of COH is presented in table 2.

The normalized random error of the magnitude factor of CSDF, $|\hat{G}_{ij}(f)|$, is,

$$\epsilon_r[|\hat{G}_{ij}(f)|] = 1/|\hat{\gamma}_{ij}|\sqrt{N_d} = 0.106. \quad [A4]$$

The standard deviation of an estimate of the phase factor of CSDF, $\hat{\theta}_{ij}(f)$, is

$$\mathrm{SD}[\hat{\theta}_{ij}(f)] \doteq (1 - \hat{\gamma}_{ij}^2)^{1/2}/|\hat{\gamma}_{ij}|\sqrt{2N_d} = 0.041(\mathrm{rad}), \quad [A5]$$

and the random error for an estimate of $\hat{\theta}_{ij}(f)$ is

$$\epsilon[\hat{\theta}_{ij}(f)] = \mathrm{SD}[\hat{\theta}_{ij}(f)]/\theta_{ij}(f) = 0.014, \quad [A6]$$

for a value of $\hat{\theta}_{ij}(f) = 170°$ which is typical of most test runs.

With the bias error of $\hat{\theta}_{ij}(f) < 0.15\%$ as already mentioned, the uncertainty for $\hat{\theta}_{ij}(f)$ is 2.8% for a 95% confidence level, and the true value lies in the following band:

$$\theta_{ij}(f) = 170 \pm 4.7(\mathrm{degrees}).$$

The overall uncertainty of $\hat{\theta}_{ij}(f)$ for other values of COH is also presented in table 2.

The random error for an estimate of the magnitude factor of TFN, $|\hat{H}_{ij}|$, is

$$\epsilon[|\hat{H}_{ij}|] = \mathrm{SD}[|\hat{H}_{ij}|]/|H_{ij}| \doteq (1 - \hat{\gamma}_{ij}^2)^{1/2}/|\hat{\gamma}_{ij}|\sqrt{2N_d} = 0.041. \quad [A7]$$

The random error of $|\hat{H}_{ij}|$ for other values of COH is presented in table 2.

The overall uncertainty of the peak time, $\tau_{max}$, and wave speed, $C_c$, is determined to be less than 7.2% for $\hat{\gamma}_{ij}^2 = 0.7$.

†ANSI/ASME PTC 19.1 1985 *Measurement Uncertainty*. American Society of Mechanical Engineers, New York.